FLOW INDUCED BY BACTERIAL CARPETS AND TRANSPORT OF MICROSCALE LOADS

AMY L. BUCHMANN*, LISA J. FAUCI†, KARIN LEIDERMAN ‡, EVA M. STRAWBRIDGE §, AND LONGHUA ZHAO ¶

Abstract.
In this paper we utilize the method of regularized Stokeslets to explore flow fields induced by 'carpets' of rotating flagella. We model each flagellum as a rigid, rotating helix attached to a wall, and study flows around both a single helix and a small patch of multiple helices. To test our numerical method and gain intuition about flows induced by a single rotating helix, we first perform a numerical time-reversibility experiment. Next, we investigate the hypothesis put forth in [6] that a small number of rotating flagella could produce "whirlpools" and "rivers" a small distance above them. Using our model system, we are able to produce "whirlpools" and "rivers" when the helices are rotating out of phase. Finally, to better understand the transport of microscale loads by flagellated microorganisms, we model a fully-coupled helix-vesicle system by placing a finite-sized vesicle held together by elastic springs in fluid near one or two rotating helices. We compare the trajectories of the vesicle and a tracer particle initially placed at the centroid of vesicle and find that the two trajectories can diverge significantly within a short amount of time. Interestingly, the divergent behavior is extremely sensitive to the initial position within the fluid.

Key words. Bacterial Carpet, Helical flagella, Method of regularized Stokeslets, Stokes flow

AMS(MOS) subject classifications. 76, 92

1. Introduction. Recent developments in microfluidic devices have enabled controlled studies and manipulation of fluid flows with length scales at the micron level [12]. Fabricated helical micromachines that are driven by magnetic actuation can move colloidal microparticles [14]. Nature's own micromachines, flagellated microorganisms, can also be used to transport loads in microfluidic devices [15]. At this length scale where inertia is negligible, viscous forces are very important and processes such as diffusion and surface tension dominate. In many microfluidic experiments that measure chemical and biological processes, mixing of the fluid within the chamber is desirable. A novel approach to microfluidic mixing and transport introduced by N. Darnton et al [6] is the use of flagellated bacteria as fluidic actuators. In this approach, bacteria are made to adhere to a substrate (see Figure 1). The adherent bacteria on this "bacterial carpet" freely rotate their flagella, which move the fluid near them and act as microscopic propellers, with no need for an external power source. Furthermore, they can live on small amounts of simple nutrients and can maintain mobility for several hours without food [9]. Methods for visualizing neighboring bacteria in a bacterial carpet have also shed light upon the distribution and orientation of individual flagella [8].

In order to control fluid transport by rotating helices, both natural and fabricated, an understanding of the fluid flow generated by an array of rotating helices is essential. Moreover, the addition of a microscale load such as a colloidal particle of non-negligible volume changes the flow dynamics, and its transport is governed by the coupled helix-vesicle system. In this paper, we present a mathematical model and numerical method that solves the full Stokes equations of zero Reynolds number flow with an array of helices emanating from a planar wall in 3D. The orientation of the axes of the helices, their geometries, their rotational frequencies and their phase differences can be specified independently. In addition, we include the transport of a deformable, finite-sized vesicle whose rigidity may be controlled by the choice of an elastic parameter.

2. Methodology. In this study, we explore the fluid flow induced by a helical flagellum attached to a planar wall and rotating in a very viscous fluid. We utilize the method of regularized Stokeslets and the image system previously derived to account for the presence of a plane wall [4, 5, 1]. We also introduce a finite-sized spherical vesicle, held together by elastic springs, into the flow field to better understand the

*University of Notre Dame, Applied and Computational Mathematics and Statistics, South Bend, IN, USA, abuchman@nd.edu

†Tulane University, Department of Mathematics, New Orleans, LA, USA, fauci@tulane.edu, NSF DMS 1043626

‡University of California Merced, Applied Math Unit, Merced, CA, USA, kleiderman@ucmerced.edu

§James Madison University, Department of Mathematics and Statistics, Harrisonburg, VA, USA, strawbem@jmu.edu

¶Case Western Reserve University, Department of Mathematics, Applied Mathematics, and Statistics, Cleveland, OH, USA lxz315@case.edu

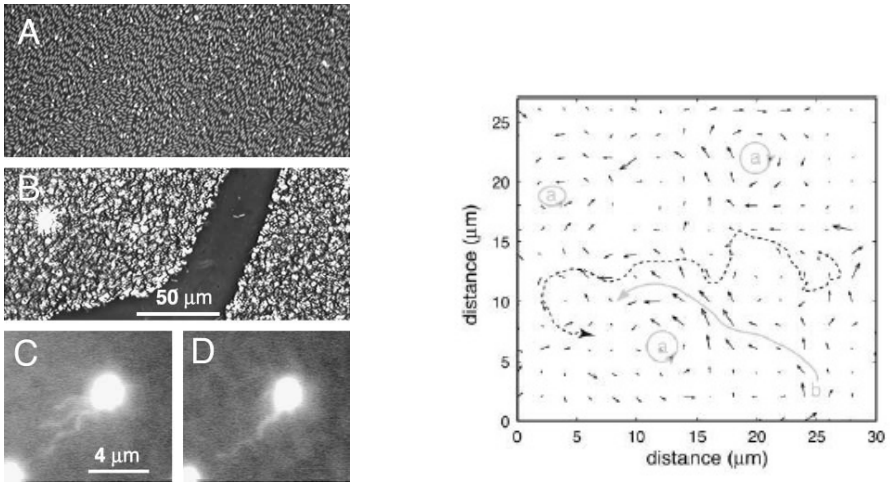

Fig. 1: Left: phase-contrast image of a bacterial carpet from [6]. The panels show (A) bacteria lying flat on the surface, (B) attached end-on, and swimming bacteria with flagella (C) unbundled and (D) bundled. Right: vector plot of velocities of the fluid just above an active carpet of bacteria where "rivers" and "whirlpools" are observed. The regions marked with 'a' indicate qualitatively observed whirlpools while the solid line labeled 'b' shows what [6] called rivers. The dotted line shows a typical path of a tracer bead. Both figures are reprinted from [6] with permission. The complete parameters for the figure are given in that original report.

ability of flagellated bacteria to transport microscale loads. Below we briefly discuss the equations of motion in this viscous regime, the method of regularized Stokeslets and its image system, and the geometry of the helical flagellum. In later sections, we will describe the solution process for treating the motion of the finite-sized vesicle in the fluid.

2.1. Stokeslets. At zero Reynolds number, the motion of an incompressible viscous fluid due to a point force at $\mathbf{x_0}$ is governed by the singularly forced Stokes equations

$$-\nabla p + \mu \Delta \mathbf{u} = -\mathbf{g}\delta(\hat{\mathbf{x}}), \tag{2.1}$$

$$\nabla \cdot \mathbf{u} = 0, \tag{2.2}$$

where p is fluid pressure, $\mathbf{u}$ is fluid velocity, μ is fluid viscosity, $\mathbf{g}$ is an arbitrary constant external force acting on the fluid, δ is the Dirac delta function, and $\hat{\mathbf{x}} = \mathbf{x} - \mathbf{x_0}$. One can think of $\mathbf{x}$ as a point of observation and $\mathbf{x_0}$ as the location of a point force where the distance between them is defined by $r = \|\mathbf{x} - \mathbf{x_0}\|$. In three spatial dimensions, the free space Stokeslet, or fundamental solution, is

$$\mathcal{S}(\hat{\mathbf{x}}) = 8\pi(-\Delta \mathbf{I} + \nabla\nabla)B(r) = \frac{\mathbf{I}}{r} + \frac{\hat{\mathbf{x}}\hat{\mathbf{x}}}{r^3}, \tag{2.3}$$

where $B(r) = -\frac{r}{8\pi}$ is the fundamental solution to the biharmonic equation $\Delta^2 B(r) = \Delta G(r) = \delta$, and $G(r)$ is the fundamental solution to Laplace's equation. The solution to Equations (2.1) and (2.2) is then given by

$$\mathbf{u}(\mathbf{x}) = \frac{1}{8\pi\mu}\mathcal{S}(\hat{\mathbf{x}})\mathbf{g}.$$

The Stokeslet describes the velocity field induced by a point force anywhere except at its own location. From Equation (2.3) one can see the singular behavior that emerges as an observation point approaches a point force. When a collection of point forces are concentrated along smooth surfaces, the velocity in terms of the Stokeslet is integrable, but if concentrated along curves in three dimensions (e.g., a slender, elastic

structure such as flagella), the velocity expression is singular. The method of regularized Stokeslets, based on a smoothing of the forces, was introduced to deal with these singularities [4, 5].

The central idea behind the method of regularized Stokeslets is to replace the singular force in Equation (2.1) with a smooth, concentrated force so that the velocity is defined everywhere, including the location of the force. This is achieved by using a radially symmetric, smooth blob function, ϕ_ϵ, that satisfies the property $\int_0^\infty r^2\phi_\epsilon(r)dr = 1/4\pi$. In Figure 2 we show a plot of a typical blob function,

$$\phi_\epsilon(r) = \frac{15\epsilon^4}{8\pi(r^2+\epsilon^2)^{7/2}}, \tag{2.4}$$

for three values of the blob parameter, ϵ. This parameter controls the effective radius of the region where the force is concentrated.

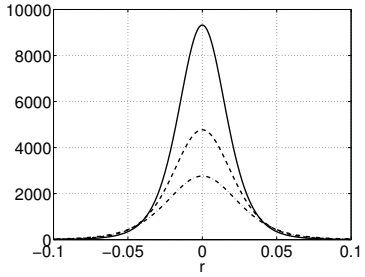

Fig. 2: Plot of the blob in (2.4) with ϵ=0.04 (solid line), ϵ=0.05 (dashed line - value used in simulations), and ϵ=0.06 (dash-dot line).

The new equations using the blob function in place of the delta function,

$$-\nabla p + \mu\nabla^2\mathbf{u} = -\mathbf{g}\phi_\epsilon(\hat{\mathbf{x}}), \tag{2.5}$$
$$\nabla\cdot\mathbf{u} = 0, \tag{2.6}$$

can be solved exactly. For a given blob function, the corresponding biharmonic function, $B_\epsilon(r)$, is defined by $\Delta^2 B_\epsilon(r) = \phi_\epsilon(r)$. The smoothed force gives rise to a regularized Stokeslet and the solution to equations (2.5) and (2.6) becomes

$$\begin{aligned}\mathbf{u}(\mathbf{x}) &= \frac{1}{8\pi}\mathcal{S}_\epsilon(\hat{\mathbf{x}})\mathbf{g}, \\ &= \left[(-\Delta\mathbf{I} + \nabla\nabla)B_\epsilon(r)\right]\mathbf{g}, \\ &= \left[H_1(r)\mathbf{I} + H_2(r)\hat{\mathbf{x}}\hat{\mathbf{x}}\right]\mathbf{g},\end{aligned} \tag{2.7}$$

where $H_1(r)$ and $H_2(r)$ are defined as

$$H_1(r) = -\frac{B_\epsilon'(r)}{r} - B_\epsilon''(r), \qquad H_2(r) = \frac{rB_\epsilon''(r) - B_\epsilon'(r)}{r^3}. \tag{2.8}$$

When a collection of regularized point forces are acting on the fluid, the velocity at any point in the fluid may be represented as a summation of these contributions. For example, given N regularized point forces, $\mathbf{f}_i$ where $i = 1\ldots N$ located at the points $\mathbf{x}_i$, the resulting velocity at any point $\mathbf{y}$ is

$$\mathbf{u}(\mathbf{y}) = \frac{1}{8\pi}\sum_{i=1}^{N}\mathcal{S}_\epsilon(\mathbf{y}-\mathbf{x}_i)\mathbf{f}_i. \tag{2.9}$$

Note that if one is interested in computing the velocity at M points in the fluid $\mathbf{y}_k$ where $k = 1 \dots M$, then equation (2.10) can used to write the velocity at each point

$$\mathbf{u}(\mathbf{y}_k) = \frac{1}{8\pi} \sum_{i=1}^{N} \mathcal{S}_\epsilon(\mathbf{y}_k - \mathbf{x}_i)\mathbf{f}_i, \tag{2.10}$$

which can then be written as a matrix equation

$$\mathbf{U} = A\mathbf{F}, \tag{2.11}$$

where, in three dimensions, $\mathbf{U}$ and $\mathbf{F}$ are vectors of length $3M \times 1$ and $3N \times 1$, respectively, and A is a $3M \times 3N$ matrix with entries that depend on the regularized Stokeslet. If, instead, the velocity $\mathbf{u}$ at the locations of the regularized point forces $\mathbf{x}_i$ is known and one is interested in the forces $\mathbf{f}_i$ that yield those velocities, one can write

$$\mathbf{u}(\mathbf{x}_i) = \frac{1}{8\pi} \sum_{j=1}^{N} \mathcal{S}_\epsilon(\mathbf{x}_i - \mathbf{x}_j)\mathbf{f}_j \tag{2.12}$$

as a matrix equation

$$\mathbf{U} = B\mathbf{F}, \tag{2.13}$$

where, in three dimensions, $\mathbf{U}$ and $\mathbf{F}$ are both vectors of length $3N \times 1$ and B is a square matrix of size $3N \times 3N$ with entries that depend on the regularized Stokeslet and the locations of the points $\mathbf{x}_i$.

2.2. Image System for a Stokeslet. The method of images is a common method used to enforce boundary conditions when solving linear PDEs in bounded or semi-infinite domains. Superposition of the free-space fundamental solution is used to obtain the fundamental solution in the bounded domain by adding an image source mirrored across the boundary. The image system for the singular Stokeslet near a plane wall was obtained in [2]. The solution procedure was based on Fourier transforms and the result was interpreted as a sum of singularity solutions (Stokeslet, Stokeslet doublet and Stokeslet potential dipole) evaluated at the image point. In this study, we use the image system for a regularized Stokeslet, previously derived in [1]. The regularized Stokeslet image system is the combination of the regularized Stokeslet, regularized Stokeslet doublet, regularized Stokeslet potential dipole, and, different from the singular image system, also includes the regularized Rotlet. The singularity solutions are evaluated at the image point across the wall to enforce the no-slip boundary condition on the wall. In this study, we use the blobs and regularized singularity solutions in the forms found in [1].

2.3. Helical Flagellum. We model helical flagella in both upright positions and tilted positions as shown in Fig. 3. The centerline of an idealized helical flagellum is defined by

$$x_c = \alpha \tanh(100s) \cos\left(\frac{2\pi s}{\lambda}\right), \tag{2.14}$$

$$y_c = \alpha \tanh(100s) \sin\left(\frac{2\pi s}{\lambda}\right), \tag{2.15}$$

$$z_c = s, \tag{2.16}$$

where $0 \le s \le L$, L is the height of the helix, α is the distance from the centerline of the helix to its axis of rotation, and λ is the helical pitch. The pitch angle, β, is related to the helical pitch by

$$\tan\beta = \frac{2\pi}{\lambda}\alpha. \tag{2.17}$$

Using a standard rotation matrix, the position of the centerline of an upright helix rotating with angular velocity $(0, 0, \omega)$, is therefore

$$\begin{bmatrix} x(t) \\ y(t) \\ z(t) \end{bmatrix} = \begin{bmatrix} \cos(\omega t) & -\sin(\omega t) & 0 \\ \sin(\omega t) & \cos(\omega t) & 0 \\ 0 & 0 & 1 \end{bmatrix} \begin{bmatrix} x_c \\ y_c \\ z_c \end{bmatrix}. \tag{2.18}$$

The position of the centerline of a tilted helix is defined by an elevation angle, ϕ, an azimuthal angle, θ, and their corresponding rotation matrices

$$\begin{bmatrix} x(t) \\ y(t) \\ z(t) \end{bmatrix} = \begin{bmatrix} \cos\theta & -\sin\theta & 0 \\ \sin\theta & \cos\theta & 0 \\ 0 & 0 & 1 \end{bmatrix} \begin{bmatrix} \cos\phi & 0 & \sin\phi \\ 0 & 1 & 0 \\ -\sin\phi & 0 & \cos\phi \end{bmatrix} \begin{bmatrix} \cos(\omega t) & -\sin(\omega t) & 0 \\ \sin(\omega t) & \cos(\omega t) & 0 \\ 0 & 0 & 1 \end{bmatrix} \begin{bmatrix} x_c \\ y_c \\ z_c \end{bmatrix}. \quad (2.19)$$

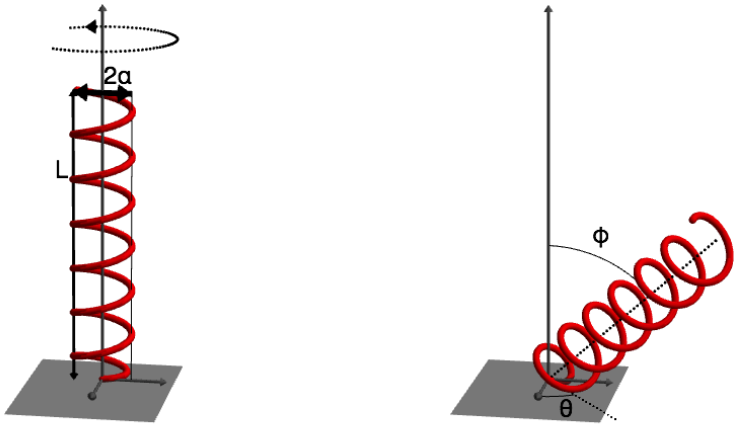

(a) Upright helix (b) Tilted helix with tilt angle ϕ

Fig. 3: Sketch of two helix positions. The specified helix parameters are height L, radius α and ratio L/λ where the pitch number, λ, is defined by a pitch angle β where $\tan\beta = \frac{2\pi\alpha}{\lambda}$. When the helix is tilted, its position is prescribed with the elevation angle ϕ and azimuthal angle θ. When $\phi = 0$, the helix is set upright. In both situations, the helix is self-rotating around its axis.

Each model helix is set to have height $10\mu m$, radius $0.25\mu m$, cross-sectional radius $0.01\mu m$, and pitch $2.5\mu m$, and is discretized into 120 points. These parameters were chosen to match the dimensions of the bacterial flagella of the experiments done in [6]. We choose the blob parameter, ϵ=0.05μm, which acts as the effective cross-sectional radius of the flagellum; this is slightly larger than the real cross-sectional radius of the bacterial flagellum [6]. With this blob parameter, we discretize each helix into 120 points. It has been shown that when using the method of regularized Stokeslets, a good choice for the discretization is one where the spacing between points is on the order of the size of the blob parameter [5, 10, 3]. The plot of the blob function with our chosen parameter is shown in Figure 2.

2.4. Nondimensionalization. We define the nondimensional variables of equations (2.5) and (2.6) as:

$$\mathbf{u}^* = \frac{\mathbf{u}}{\mathcal{U}}, \quad \mathbf{x}^* = \frac{\mathbf{x}}{\mathcal{L}}, \quad p^* = \frac{p}{\mathcal{P}}, \quad \mathbf{g}^* = \frac{\mathbf{g}\mathcal{L}^3}{\mathcal{F}}, \quad t^* = \frac{t}{\mathcal{T}},$$

where $\mathcal{U}, \mathcal{L}, \mathcal{P}, \mathcal{F}, \mathcal{T}$ are the characteristic velocity, length scale, pressure, force and time scale, respectively. We choose $\mathcal{U}$=10 μm/s, $\mathcal{L}$=10 μm, $\mathcal{T}$=1 second, $\mathcal{P}$=μ $\mathcal{U}/\mathcal{L}$, and $\mathcal{F}$=μ $\mathcal{U}\mathcal{L}$, where μ=1$\times10^{-3}$kg m^{-1}s^{-1} is the dynamic viscosity of water. Using these nondimensional variables, equations (2.5) and (2.6) simplify to:

$$-\nabla p^* + \nabla^2 \mathbf{u}^* = -\mathbf{g}^* \phi_\epsilon(\hat{\mathbf{x}}), \quad (2.20)$$

$$\nabla \cdot \mathbf{u}^* = 0, \quad (2.21)$$

and these are the equations that we actually solve in the numerical experiments that follow.

2.5. Coupled Helix-Vesicle System. In our numerical experiments, we will model one or more rotating helices attached to a wall, propelling a Stokesian fluid. In some simulations, these helices will also be interacting with a finite-sized spherical vesicle. In this section we describe the equations and methodology to model the coupled system.

The surface of the spherical vesicle is discretized into N points using Spherical Centroidal Voronoi Tessellation (SCVT) and the package STRIPACK [7, 11]. The SCVT algorithm positions a specified number of points on a unit sphere so that the points are approximately equally spaced and the Delaunay triangulation of these same points on the unit sphere is obtained using STRIPACK. The arc length of each of the N_h helices is discretized into M equally-spaced points, where $N_h = 1$ or 2, is the number of helices. The addition of a vesicle and helices in a Stokes flow result in new, governing equations for fluid motion:

$$-\nabla p + \mu\nabla^2\mathbf{u} + \sum_{i=1}^{N} \mathbf{f}_i\phi_\delta + \sum_{j=1}^{M\cdot N_h} \mathbf{g}_j\phi_\delta = 0, \tag{2.22}$$

$$\nabla \cdot \mathbf{u} = 0. \tag{2.23}$$

Here, $\mathbf{f}$ and $\mathbf{g}$ are the forces on the fluid from the vesicle and helices, respectively, both scaled by the same characteristic force, $\mathcal{F}$. To calculate the velocity $\mathbf{u}$ at any point in the domain, one must first know the forces $\mathbf{f}$ and $\mathbf{g}$. The forces concentrated at the discretized points on the vesicle are due to elastic springs that hold it in its spherical shape. These elastic forces are computed using specified spring constants and resting lengths between points. In contrast, the forces along the length of a helix are unknown. However, the rotational velocities along each helix are specified. To find these forces, we exploit linearity of the equations, and split the velocity and the pressure *at any spatial location* as $\mathbf{u} = \mathbf{u}_1 + \mathbf{u}_2$ and $p = p_1 + p_2$ such that

$$-\nabla p_1 + \mu\nabla^2\mathbf{u}_1 + \sum_{i=1}^{N} \mathbf{f}_i\phi_\delta = 0, \tag{2.24}$$

$$\nabla \cdot \mathbf{u}_1 = 0,$$

and

$$-\nabla p_2 + \mu\nabla^2\mathbf{u}_2 + \sum_{j=1}^{M\cdot N_h} \mathbf{g}_j\phi_\delta = 0. \tag{2.25}$$

$$\nabla \cdot \mathbf{u}_2 = 0.$$

As described in the text around equation (2.11), the forces and velocities can be related via the matrix equations $\mathbf{U}_1 = A_1\mathbf{F}$ and $\mathbf{U}_2 = A_2\mathbf{G}$. If we consider this relationship at k discrete locations in space, then A_1 is a matrix of size $3k \times 3N$ and $\mathbf{U}_1$ and $\mathbf{F}$ are vectors of size $3k \times 1$ and $3N \times 1$, respectively. The vector $\mathbf{U}_1$ consists of the k, sequentially-stacked, velocities, $\mathbf{u}_1$, and $\mathbf{F}$ consists of the N, sequentially-stacked, point forces located on the vesicle, $\mathbf{f}_i$, that are induced on the fluid. Similarly, $\mathbf{U}_2$ is a vector of the velocities, $\mathbf{u}_2$, and $\mathbf{G}$ is a vector of the forces located on the helices, $\mathbf{g}$, that are induced on the fluid. The entries of the matrices A_1 and A_2 are computed using the regularized Stokeslet [4, 5], the fundamental solution to (2.24) and (2.25). For clarity, we note again that one can represent the velocity at *any* location with $\mathbf{u} = \mathbf{u}_1 + \mathbf{u}_2$. As another example, the velocity at points located on the vesicle, call them $\mathbf{u}_v$, can be split into $\mathbf{u}_v = \mathbf{u}_1 + \mathbf{u}_2$. With this, the velocities $\mathbf{u}_1$ would represent the velocity at points *on the vesicle* induced by the forces *on the vesicle* and the velocities $\mathbf{u}_2$ would represent the velocity at points *on the vesicle* induced by the forces *on the helices*. Essentially, every velocity can be decomposed into pieces that are separately affected by the vesicle and the helices.

The algorithm proceeds as follows:

1. Calculate the forces on the vesicle $\mathbf{F} = (\mathbf{f_1}, ..., \mathbf{f_N})$ using Equation (2.26) with a fixed spring constant, k, and fixed rest lengths $\triangle s_j$ since the spherical elastic vesicle is held together by N points connected

by Hookean springs. The rest lengths of the springs, $\triangle s_{ij}$ for point $\mathbf{X}_i$ connected to all other points $\mathbf{X}_j, j = 1, ..., N$, are set to be the initial distances between points in a spherical configuration. For example, given a Hookean spring between two points located at $\mathbf{X}$ and $\mathbf{Y}$ with rest length $\triangle s$, the general form for the force at either end of the Hookean spring is:

$$\mathbf{f}_{spring} = \pm\, k \left(\frac{||\mathbf{X} - \mathbf{Y}||}{\triangle s} - 1 \right) \frac{\mathbf{X} - \mathbf{Y}}{||\mathbf{X} - \mathbf{Y}||}. \tag{2.26}$$

The total force $\mathbf{f}_i$ at point $\mathbf{X}_i$ on the vesicle is the sum of all of the spring forces resulting from all springs connected to the point $\mathbf{X}_i$.

2. Use the forces $\mathbf{F}$ calculated in Step 1 and $\mathbf{U}_1 = A_1\mathbf{F}$ to compute $\mathbf{U}_1$, the velocity at points located on the helices due to the vesicle.
3. Use $\mathbf{U}_1$ calculated in Step 2 and then compute $\mathbf{U}_2 = \mathbf{U}_h - \mathbf{U}_1$. Use $\mathbf{U}_2 = A_2\mathbf{G}$ to solve for $\mathbf{G}$, the forces at points located on the helices.
4. Use $\mathbf{U} = A_1\mathbf{F} + A_2\mathbf{G}$, with $\mathbf{F}$ and $\mathbf{G}$ calculated in steps 1-3, at points located on the vesicle to update the location of the points on the vesicle using
$$\frac{d\mathbf{X}_i}{dt} = \mathbf{U}(\mathbf{X}_i, t).$$
5. Use $\mathbf{U} = A_1\mathbf{F} + A_2\mathbf{G}$ to find the velocity at any other desired spatial location (for instance to update positions of Lagrangian fluid particles or to assemble velocity fields).

We note that in the cases where we are interested in the flows created by helices with no immersed vesicle, the forces $\mathbf{F}$ above are identically zero, as are the velocities induced by the vesicle on the helices $\mathbf{U}_1$.

3. Numerical Experiments. In this section, we present three numerical experiments to explore flows generated by rotating helices attached to a wall. First, we illustrate the reversibility of Stokes flow using our numerical method and model helix setup. Next we show that multiple helices with varying tilt and phase, but not without, produce "rivers" and "whirlpools" in regions of the velocity fields as seen in experiments [6], see Figure 1. Finally, we investigate the motion of a finite-sized vesicle induced by rotating helices.

3.1. Reversibility of Stokes Flow. Because the Stokes equations we model do not depend on time, except through a time-dependent force or boundary condition, their solutions represent a sequence of steady states and can be found without knowing solutions at any other time. For velocity, $\mathbf{u}$, and pressure, p that solve the Stokes equations with zero forcing, i.e., Equations (2.1) and (2.2) with $\mathbf{g} = \mathbf{0}$, it is clear that $-\mathbf{u}, -p$ solve the same homogeneous equations which means that a reversed flow is a possible physical solution. It follows that if $\mathbf{u}, p$ solve equations (2.1) and (2.2) with nonzero force, $\mathbf{g}$, then $-\mathbf{u}, -p$ solve the equations forced with $-\mathbf{g}$.

G.I. Taylor conducted a famous experiment that elegantly displayed time-reversibility of the Stokes equations [13]. In that experiment, a drop of dye was injected in a viscous fluid between two cylinders. The interior cylinder was turned multiple times until the drop of dye vanished to the naked eye. Then the interior cylinder was turned the opposite direction, thus imposing force in the opposite direction, and after the same number of turns, but not necessarily at the same speed, the drop of dye reappeared in the exact position from which it started. To check our numerical method and to gain intuition about flows induced by a single rotating helix attached to a wall, we now present a numerical time-reversibility experiment.

In our experiment, a collection of 400 tracer particles (passive particles that move with the local velocity but do not affect it) in a spherical configuration is placed adjacent to a single rotating helix anchored to a wall. The tracer particles are initialized on the surface sphere with center at (0,0,5) μm and radius 0.5 μm. We place the base of the helix at (1,0,0.0505), rotate it ten times clockwise (Figure 4 a-c) and then rotate it ten times in the counter-clockwise direction (Figure 4 d-f). Indeed, we see that the tracer particles spread out and then go back to the original position, with negligible numerical error. Figure 4g shows the top view of the tracer particles after the first 10 rotations. To see the flow fields that are generated by a rotating helix, we plot the three-dimensional velocity vectors on the plane y=0 in Figure 4h, and on the plane z=5 in Figure 4i.

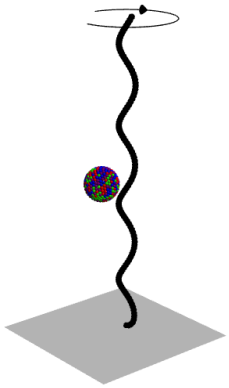

(a) T=0

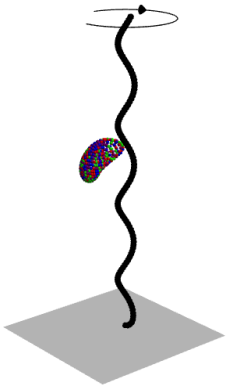

(b) T=5

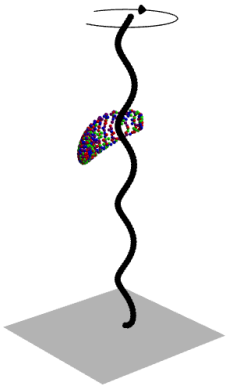

(c) T=10

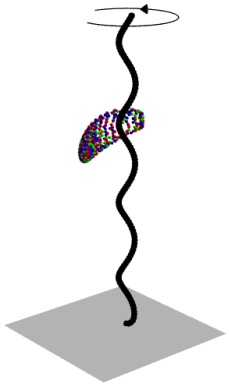

(d) T=10 (reverse direction)

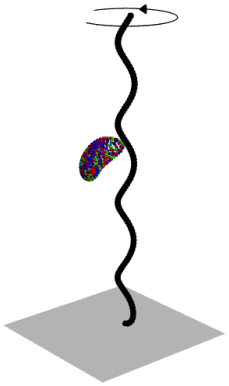

(e) T=15

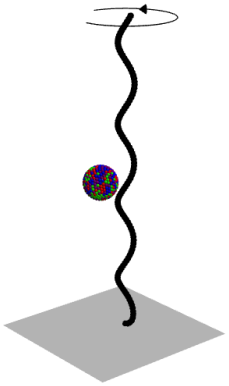

(f) T=20

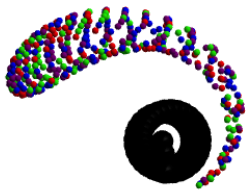

(g) Top view at T=10.

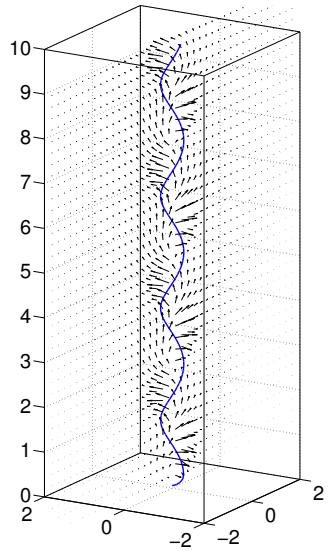

(h) Velocity field through $y = 0$ plane.

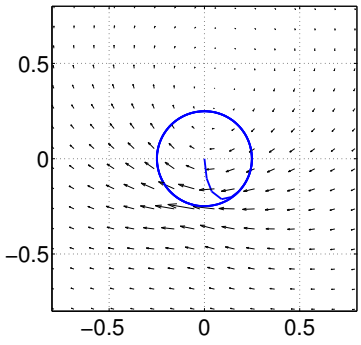

(i) Velocity field through $z = 5$ plane

Fig. 4: Reversibility (a-g): snapshots of tracer particles initialized on a spherical surface adjacent to a rotating helix. $T = 0, 5, \cdots, 20$ represents the number of times the helix has been rotated in time. At $T = 10$, the direction of rotation is reversed. Velocity fields through the y=0 (h) and z=5 (i) planes.

3.2. Rivers and Whirlpools. Darnton *et al.* [6] adhered flagellated bacteria, that freely rotate their flagella, to a substrate. The rotating flagella move the fluid around the bacteria and act as microscopic propellers. In that study, 1 μm beads were tracked in the flow just above the bacteria. Velocity fields were calculated from video that tracked the beads' motion. In certain regions of the observed velocity fields, flow seemed to behave like "rivers" and "whirlpools", see Figure 1. The whirlpools were regions where the flow looked circular and the rivers transported beads in an almost straight line. The rivers seemed to be constructed from suitably-spaced nearby whirlpools rotating in opposite directions. The authors suggested that a whirlpool could be created by a small number of coordinated flagella aligned predominantly normal to the surface to which they are attached.

We investigate this hypothesis and simulate flows induced by multiple rotating helices attached to a wall. In addition, we set tilt angle and rotation phase as parameters. We place 16 equally-spaced, identical helices attached to a wall and compute the flows from three distinct rotating helix configurations: i) all helices upright and rotating with the same phase, ii) all helices upright and rotating with phases randomly chosen from a uniform distribution on $[0, 2\pi)$, and iii) each helix is prescribed a small randomly-chosen tilt angle by selecting the elevation angle, ϕ, and an azimuthal angle, θ, from a uniform distribution of $[0, \pi/36]$ and a randomly-chosen phase selected from uniform distribution on $[0, 2\pi)$. In all cases, the helices rotate in a clockwise direction, and the bases of adjacent helices are spaced 1.5 μm apart.

Figure 5 illustrates configuration i, ii, iii in the top, middle, and bottom row of the figure, respectively. We also present a side view of the helices (left column), top view of the helices (middle column) and the resulting velocity field in the plane that intersects the top of the helices (right column). In the top view, the line that follows the radius of each helix represents the bottom portion of the helix that attaches to the wall and also aids in identification of the rotation phase.

The upright helices that rotate with the same phase (configuration i, top row of Figure 5) generated flows with fairly uniform structure and no river/whirlpool behavior was observed. The flow behavior is dramatically altered when the rotation phases of each helix is specified at random (configuration ii, middle row of Figure 5). Rivers and whirlpools are induced in this case and we highlight a few trajectories with red dotted lines to clearly identify the structure in the flow. Similar flows were also obtained when both the tilt angle and rotation phases were specified at random (configuration iii, bottom row of Figure 5). Our results suggest that small numbers of flagella can indeed produce whirlpools as long as they are out of phase.

3.3. Transport of a Finite-Sized Vesicle. Darnton *et al.* [6] compute velocity fields by tracking the motion of tracer beads with approximate radii of 1 μm. Other flagellated microorganisms have been shown to transport loads approximately 1-6 μm in diameter in microfluidic devices [15]. To better understand the transport of microscale loads, we model a fully-coupled helix-vesicle system within a viscous fluid. With this model, we are able to compare the transport of an elastic, finite-sized vesicle (with volume) to the transport of passive tracer particles through flows induced by rotating flagella attached to a wall.

3.3.1. A Vesicle and a Single Rotating Helix. We model a vesicle together with a single rotating helix, attached to a wall, in a viscous fluid. The radius of the spherical vesicle is set to 0.05 μm and its surface is discretized into 400 points. To hold the spherical shape, the points are held together by elastic springs as described in (2.26) with nondimensional spring constant $k = 0.01$. For this study, the helix is placed in an upright position with base located at (1,0,0) μm, and then it is rotated clockwise with angular velocity (0,0,2π) and frequency 1 Hz for 100 rotations. The vesicle is initially placed adjacent to the helix so that its center is located at (0,0,5) μm.

To gain some intuition, we begin by presenting results for a spherical cloud of passive tracer particles in the presence of the rotating helix, as in our reversibility experiment previously described. For direct comparison, the tracer particles are initialized at the same location where the points on the vesicle are initialized. Figure 6 shows snapshots of this situation. Figures 6a-6d show the top views at times T that correspond to 0, 40, 60 and 100 full rotations of the helix. Figures 6e-6j show the side views at times T that correspond to 0, 20, 40, 60, 80, and 100 full rotations of the helix. One can clearly see that the tracer particles have spread out

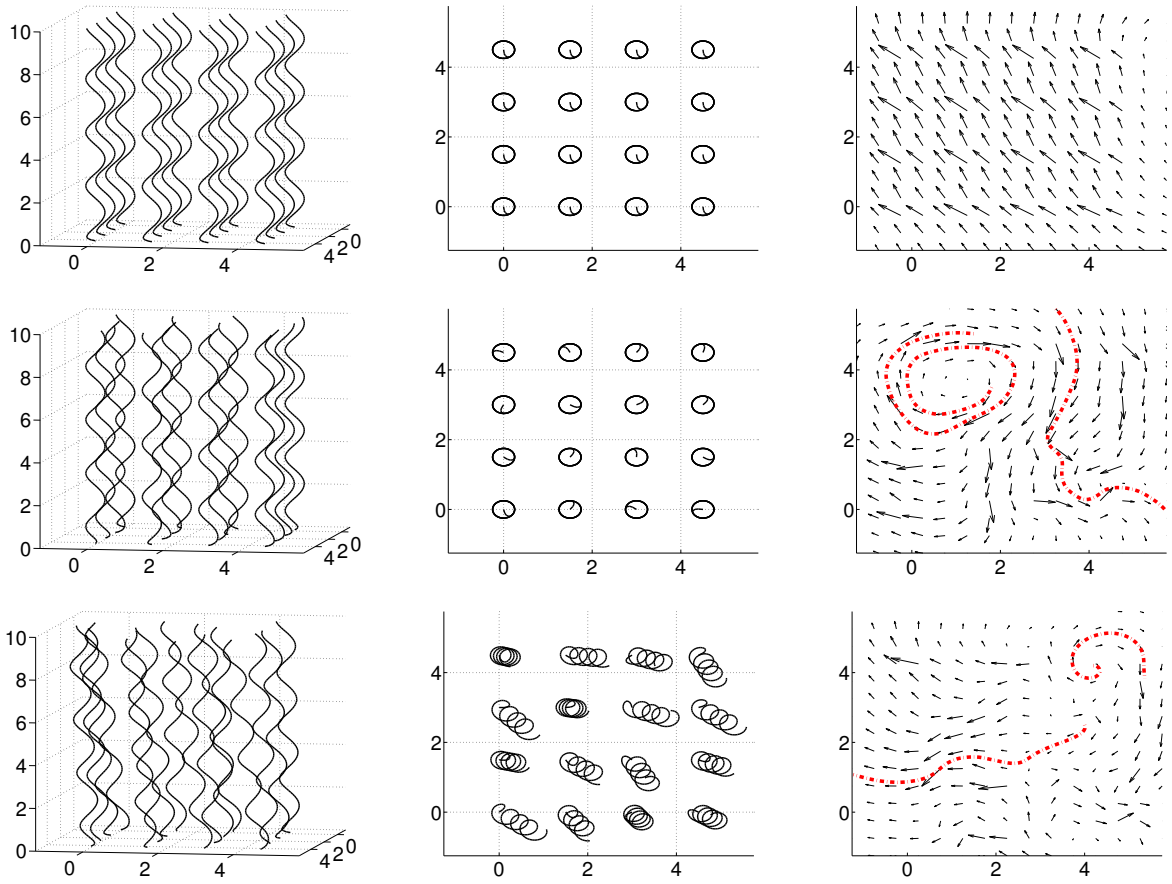

Fig. 5: Side view (left column) and top view (center column) of helices and the resulting velocity fields on the horizontal plane intersecting the top of the highest helix (right column). Each row shows a different configuration where the tilt and phase of the helices were varied. Top row: upright helices with same phases. Middle row: upright helices rotating with randomly-chosen phases. Bottom row: randomly-tilted helices with randomly-chosen phases. Thick dashed lines are chosen trajectories in the flow that show river and whirlpool behavior. Numbers on the axes are distance in μm.

a significant amount by being wrapped around the helix while also being pushed upward.

In Figure 7 we present snapshots of the vesicle together with a single rotating helix attached to a wall. Figures 7a-7d show the top views at times T that correspond to 0, 40, 60 and 100 full rotations of the helix. Figures 7e-7j show the side views at times T that correspond to 0, 20, 40, 60, 80, and 100 full rotations of the helix. Similar to the tracer particles, the vesicle rotates around the helix as it is pushed upward. But how different are the trajectories of a tracer particle and a vesicle with non-zero volume? Can one model vesicle transport by simply tracking a passive tracer particle? To answer this question, we compare the trajectory of the centroid of a vesicle with non-zero volume and, in another simulation, the trajectory of a single passive tracer that is initially placed at same spatial position as was the centroid of the vesicle.

In Figure 8, we compare the trajectory of the *centroid* of the vesicle to the trajectory of a tracer particle initially placed at the centroid of the vesicle. The left plot compares the $x-$ and $y-$coordinates of the trajectories while the right plot compares the $z-$component of the trajectories. For the first 30 rotations there is almost no difference in any of the trajectories, but after 30 rotations the $x-$component of the trajectories

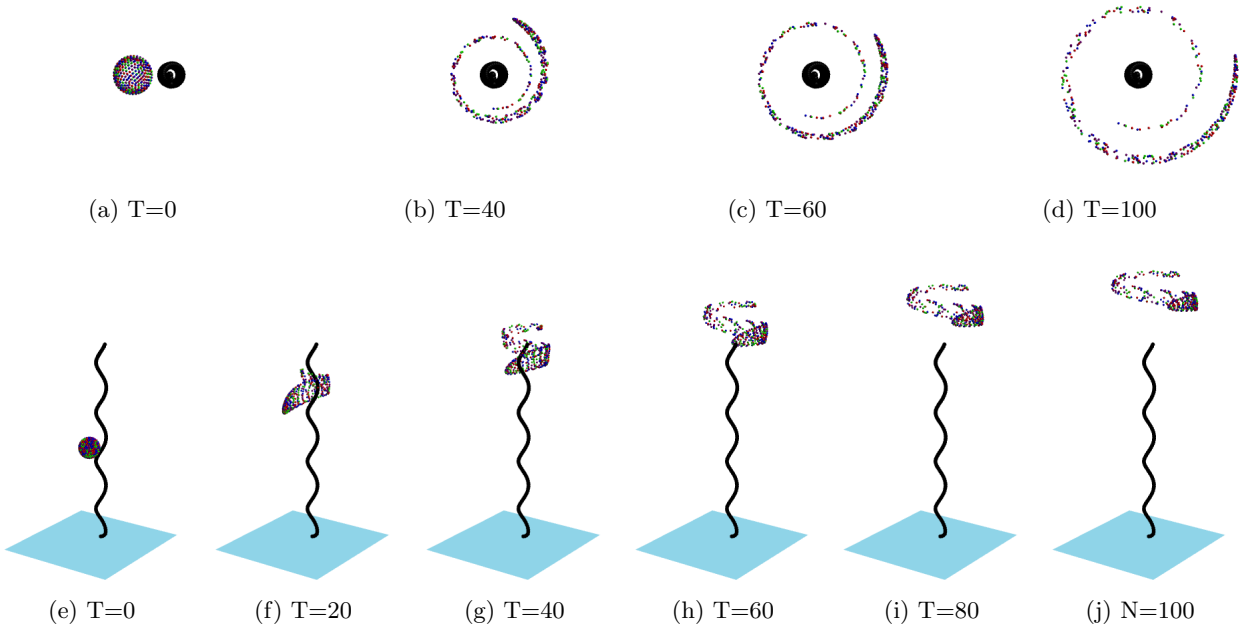

(a) T=0 (b) T=40 (c) T=60 (d) T=100

(e) T=0 (f) T=20 (g) T=40 (h) T=60 (i) T=80 (j) N=100

Fig. 6: Snapshots of tracer particles driven by a single rotating helix attached to a wall. T is the time that corresponds to number of helix rotations.

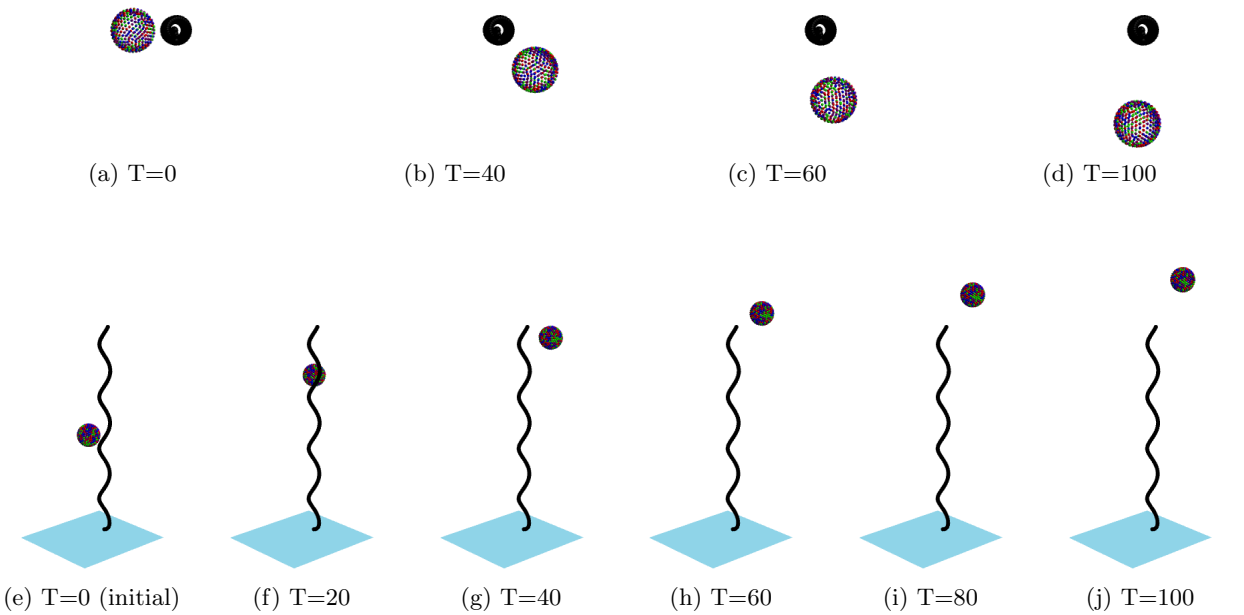

(a) T=0 (b) T=40 (c) T=60 (d) T=100

(e) T=0 (initial) (f) T=20 (g) T=40 (h) T=60 (i) T=80 (j) T=100

Fig. 7: The motion of a vesicle induced by a single rotating helix attached to a wall. T is the time that corresponds to number of helix rotations and the nondimensional spring constant in (2.26) is set to $k = 0.01$.

begin to diverge. We show here that the vesicle is being pushed outward in the $x-$direction, further away from the helix than the tracer particle. To further explore this phenomena, we increased the spring constant in the Hookean springs placed between points on the surface of the vesicle. This effectively makes it harder to deform the vesicle from its spherical shape. In Figure 9, we compare the trajectories of the *center* of vesicles with nondimensional spring constants $k = 0.01$ and $k = 1$ to the tracer particle. The left plot compares the $x-$ and $y-$coordinates of the trajectories while the right plot compares the $z-$component of the trajectories. Due to the higher spring constant the timestep was decreased to maintain stability in the explicit numerical integration. We compare the trajectories for the first 10 rotations of the helix. Even in this short time, one can see that as the spring constant increases, the discrepancy in the $x-$component of the trajectories also increases.

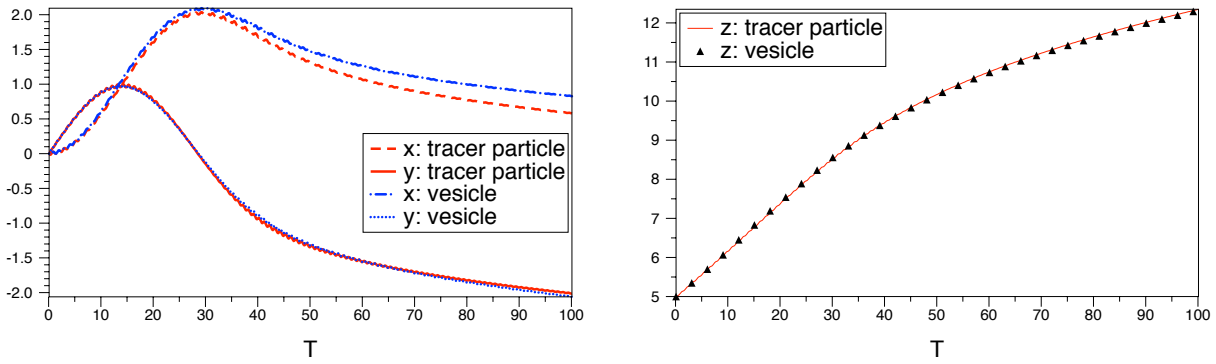

Fig. 8: Single helix: comparison of the $x-, y-$, and $z-$components of the trajectories of the tracer particle and the centroid of the vesicle. The nondimensional spring constant, k, for the vesicle is set to 0.01. T is the time that corresponds to number of helix rotations.

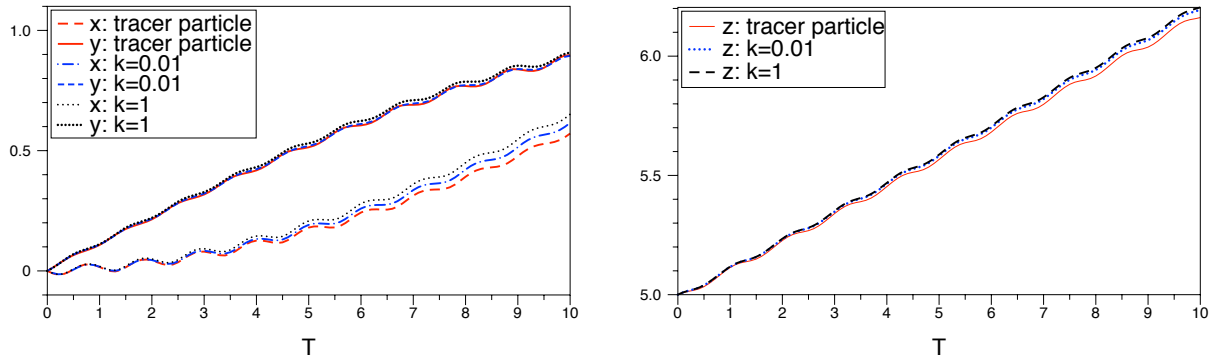

Fig. 9: Single helix: comparison of the $x-, y-$, and $z-$components of the trajectories of the center of mass of the cloud of tracer particles and the center of vesicles with nondimensional spring constants $k = 0.01$ and $k = 1$. T is the time that corresponds to number of helix rotations.

3.3.2. A Vesicle and Two Rotating Helices. We have shown that the spring constant used to model the vesicle plays a role in the coupled helix-vesicle system. As the spring constant was increased, a discrepancy in vesicle trajectories was captured after just a small number of helix rotations. But in each of those cases, the trajectories were similar in that they were moving in the same direction. In this section, we explore the effect of competing flows, that is, how does a vesicle or particle trajectory change in the presence of two rotating helices? Are there regions of the flow field between the helices where the vesicle or particle is being 'pulled' in opposite directions? If so, how different are the trajectories of a vesicle and a tracer?

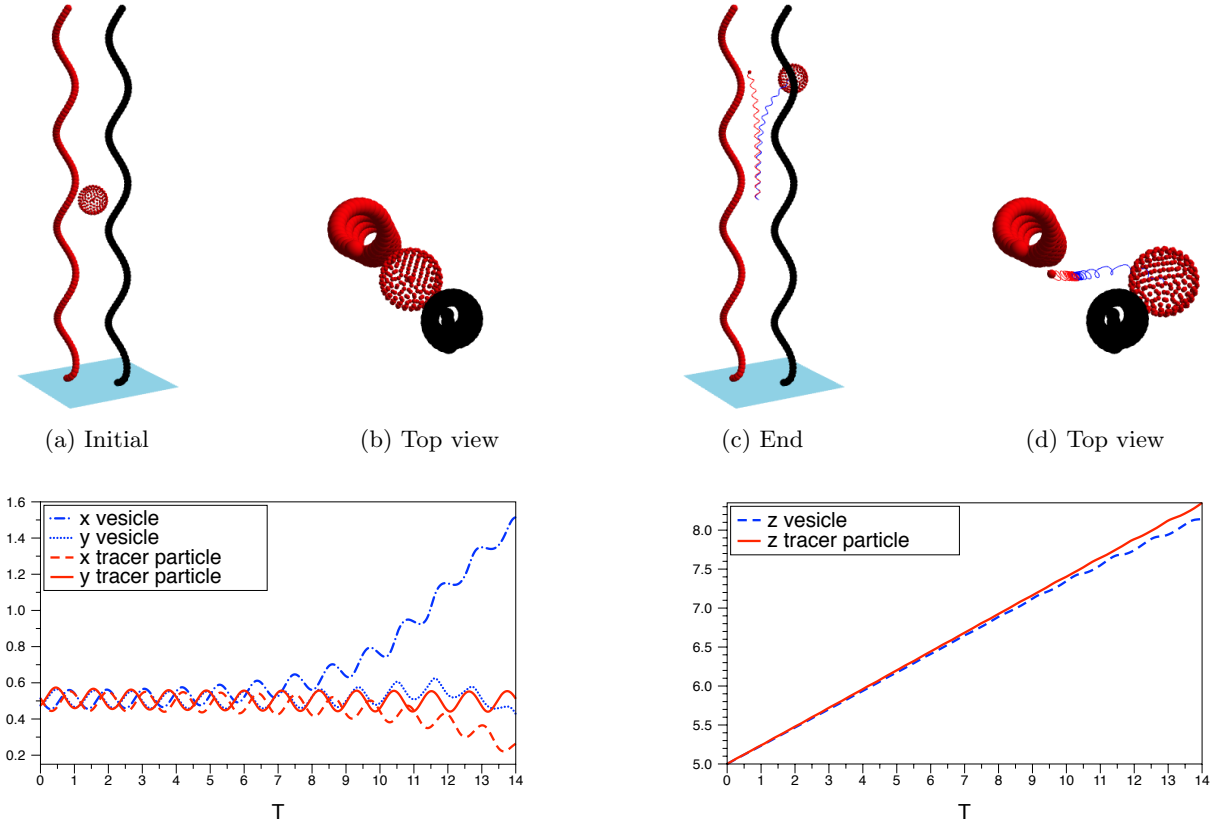

(a) Initial (b) Top view (c) End (d) Top view

Fig. 10: Top row: snapshots of the top and side view of a vesicle interacting with two rotating helices attached to a wall. Top left is initial configuration and top right is the end configuration. Trajectories of the tracer particle and the centroid of the vesicle are tracked in space. Bottom row: comparison of the $x-, y-$, and $z-$components of the trajectories of the tracer particle and the vesicle centroid. The nondimensional spring constant, k, is set to 1. T is the time that corresponds to number of helix rotations.

In this simulation, we place a vesicle, modeled as in the previous section, between two rotating helices attached to a wall. The helix parameters are the same as in the case with a single helix but now we include two helices and the location of their bases are set to $(1, 0, 0)$ and $(0, 1, 0)$. To avoid intersection of the vesicle and the helices, the spherical vesicle radius is set to $0.375\mu m$. The number of points distributed on the sphere is 225. The center of the vesicle is initialized at $(0.514, 0.475, 5)\mu m$ and this places it almost exactly between the two helical axes. Both helices are rotated in the clockwise direction with the same rotation phase, and with angular velocity $(0,0,2\pi)$ and frequency 1 Hz.

The top row of Figure 10 shows placement of the helices and trajectories of both the tracer particle and the vesicle. The bottom row shows the comparison of the $x-, y-$, and $z-$components of these trajectories. We can see from the plots in the bottom row that the trajectories begin to significantly diverge after about 6 rotations. In fact, we see that the vesicle is pushed in one direction while the tracer particle is pushed in an almost opposite direction. This behavior is very different than what was observed in the single helix case. We have found that there are interesting flow structures around multiple helices that act as separatrices between nearby tracer particles whose paths will eventually diverge. We plan to further investigate the rich dynamics of these flow fields in more detail in a future study.

4. Summary. In this paper we have utilized the method of regularized Stokeslets to explore flow fields induced by rotating flagella attached to a wall. First, we tested and calibrated our method by performing a reversibility test. In that test, we rotated a helix ten times forward and ten times backward to find that a cloud of tracer particles displaced from their starting positions as the helix rotated in one direction returned to their starting positions as the helix rotated back in the opposite direction. Next, we found that we could produce "whirlpools" and "rivers" around a small patch of sixteen helices when they were rotating out of phase. In the last section, we modeled a coupled helix-vesicle system in which a vesicle held together by elastic springs was placed in the flow along with one or two rotating helices. With this model, we compared the transport of the vesicle to the transport of a passive tracer particle through flows induced by one and two rotating helices. We found that, using the same initial positions, the trajectories of the vesicle could diverge significantly from the trajectory of the tracer particle and that this divergent behavior was extremely sensitive to the initial starting positions. In this example, the deviation in the paths is more pronounced initially in the x component, rather than the y component of the position, due to the initial placement of the vesicles/tracer particles between the two helices and the placement of the helices. We note that the largest difference does occur in the components perpendicular to the helical axis, rather than parallel to this axis. We have also observed that these discrepancies are more strongly observed when the tracer or vesicle is placed at a height (z-value) between the floor and the top of the helix, which is where the perpendicular forcing due to the spinning helix is strongest.

We also investigated trajectories of multiple tracer particles with similar initial positions and found that their trajectories could also diverge significantly without the presence of a vesicle (data not shown). This implies that there are interesting dynamics within the flows induced by multiple rotating helices, even without the coupling of the vesicle with non-zero volume. However, further investigation of the effect of a vesicle on the flow dynamics is needed. In the near future, we plan to do a more detailed study of the flow dynamics for cases in which we vary the number of helices, their rotation phases, and the elastic stiffness of the vesicle.

5. Acknowledgements. Authors gratefully acknowledge the Institute for Mathematics and its Applications for their support and the organizers of WhAM! A Research Collaboration Workshop for Women in Applied Mathematics, Dynamical Systems with Applications to Biology and Medicine.

REFERENCES

[1] J. Ainley, S. Durkin, R. Embid, P. Boindala, and R. Cortez, The method of images for regularized stokeslets, J. Comput. Phys., 227 (2008), pp. 4600–4616.
[2] J. R. Blake, A note on the image system for a Stokeslet in a no-slip boundary, Proc Camb Phil Soc, 70 (1971), pp. 303–310.
[3] E. Bouzarth and M. Minion, Modeling slender bodies with the method of regularized stokeslets, J. Comput. Phys., 230 (2011), pp. 3929 – 3947.
[4] R. Cortez, The method of regularized stokeslets, SIAM J. Sci. Comput., 23 (2001), p. 1204.
[5] R. Cortez, L. Fauci, and A. Medovikov, The method of regularized stokeslets in three dimensions: analysis, validation, and application to helical swimming, Phys. Fluids, 17 (2005), p. 031504.
[6] N. Darnton, L. Turner, K. Breuer, and H. Berg, Moving fluid with bacterial carpets, Biophys. J., 86 (2004), pp. 1863–1870.
[7] Q. Du, M. Gunzburger, and L. Ju, Constrained centroidal voronoi tessellations for surfaces., SIAM J. Sci. Comput., 24 (2003), pp. 1488–1506.
[8] W. Hesse and M. Kim, Visualization of flagellar interactions on bacterial carpets, J. Microscopy, 233 (2009), pp. 302–308.
[9] M. Kim and K. Breuer, Use of bacterial carpets to enhance mixing in microfluidic systems, J. Fluids Engr., 129 (2007), p. 319.
[10] H. Nguyen and R. Cortez, Reduction of the regularization error of the method of regularized stokeslets for a rigid object immersed in a three-dimensional stokes flow, Commun. Comput. Phys., 15 (2014), pp. 126 – 152.
[11] R. Renka, Algorithm 772, stripack: Delaunay triangulation and voronoi diagrams on the surface of a sphere., ACM Trans. Math. Soft., 23 (1997), pp. 416–434.
[12] H. Stone, A. Stroock, and A. Ajdari, Engineering flows in small devices: Microfluidics toward a lab-on-a-chip, Annu. Rev. Fluid Mech., 36 (2004), pp. 381–411.
[13] G. I. Taylor, Low reynolds number flows. VHS produced by Educational Services Incorporated under the direction of the National Committee for Fluid Mechanics Films. Chicago, Illinois: Encyclopaedia Britannica Educational Corporation, 1972.
[14] S. Tottori, L. Zhang, K. Krawczyk, A. Franco-Obregon, and B. Nelson, Magnetic helical micromachines: fabrication, controlled swimming, and cargo transport, Adv. Mater., 24 (2012), pp. 811–816.

[15] D. Weibel, P. Garstecki, D. Ryan, W. DiLuzio, M. Meyer, J. Seto, and G. Whitesides, Microoxen: Microorganisms to move microscale loads, Proc. Natl. Acad. Sci., 102 (2005), pp. 11963–11967.